PHYSICAL REVIEW B **105**, 085143 (2022)

Imaging of current crowding effect across the metal to insulator transition in a $NdNiO_3$ thin film with thickness gradient

Nirmal Roy,[1] Sayantan Ghosh,[1] Suprotim Saha,[1] G. L. Prajapati,[2] Rahul Dagar,[2] D. S. Rana,[2,*] and S. S. Banerjee[1,†]
[1]*Indian Institute of Technology Kanpur, Kanpur, Uttar Pradesh 208016, India*
[2]*Indian Institute of Science Education and Research Bhopal, Bhopal 462066, India*

(Received 11 August 2021; revised 7 February 2022; accepted 10 February 2022; published 24 February 2022)

The metal-insulator transition (MIT) phenomenon in materials is associated with a complex interplay of electronic correlations, magnetism, and strain effects. We image the current distribution around MIT in $NdNiO_3$ thin film with a thickness gradient. Above the MIT temperature, we observe a homogeneous current distribution implying the film is uniformly metallic. Below the MIT temperature, an insulating phase forms and spreads from the thicker to thinner regions of the film, leading to a nonuniform current distribution. A thickness variation induced strain distribution causes a spread in the local MIT temperature across the film. Our analysis shows the bulk resistance represents changes in the area of the metallic phase across the MIT. Our study suggests that the MIT in the nickelate film is a first-order transition from a paramagnetic non-Fermi-liquid metallic to an antiferromagnetic insulating phase. Strain distribution across the film broadens the transition.

DOI: 10.1103/PhysRevB.105.085143

I. INTRODUCTION

Metal-insulator transition (MIT) phenomenon continues to be an active area of research [1–3]. This transition is sensitive to variation in carrier concentration [4,5], structure [6–8], magnetic state [9,10], strain [11], pressure [12], or externally applied magnetic field [2]. Imaging studies in different materials have revealed that the MIT is associated with a nanoscale phase separation between metallic and insulating phases, with each phase having a different magnetic order [13–17]. Whether the phase separation is strain driven or intrinsic has remained a complex issue. Rare-earth nickelates ($R\text{NiO}_3$, $R =$ ($\neq$ La), Pr, Nd, Sm, Eu) are an interesting class of strongly correlated materials exhibiting MIT [8,18–23]. Nickelates' MIT temperature (T_{MI}) is tunable via rare-earth ion substitution, hydrostatic pressure, or epitaxial strain [10,18,24]. The high sensitivity to structural distortions makes these materials suitable for strain transducers and thermal switches [7,10,25]. In nickelates, there are alternating ferromagnetic and antiferromagnetic couplings among neighboring Ni ions [26–28]. Among these, $NdNiO_3$ (NNO) is a fascinating material that exhibits structural, electronic, and magnetic transition around T_{MI} [7,10,25]. The effect of film thickness and deposition temperature on MIT has been extensively studied [29,30]. The MIT in thin films of NNO shows nanoscale phase separation and striped nanodomain structure along the atomic terraces, indicating a strong coupling between structural and electronic degrees of freedom in this system [17,31]. We explore here the effect of strain on the MIT transition due to nonuniform thickness variation.

We use the self-field magneto-optical-imaging (SF-MOI) technique to image the current distribution across an average MIT temperature, $T_{MI}^{\text{avg}} = 124$ K in NNO film on $LaAlO_3$ (LAO) substrate. The T_{MI}^{avg} represents the average MIT seen from bulk measurement techniques like magnetization and electrical transport measurements which measure the average response of a sample. The film has a higher thickness on the left side compared to the right. Our current imaging studies show the onset of spatially inhomogeneous current distribution at $T < T_{MI}^{\text{avg}}$. For $T < T_{MI}^{\text{avg}}$ there is a nucleation and growth of the insulating (In) phase within a predominantly metallic (M) phase. The M-phase first transforms into the In phase in the film's highest thickness region and subsequently in the lower thickness regions. Observation of the current crowding effect reveals a sliver of M phase surviving in the thinnest region on the film well below the MIT. The behavior of the bulk resistance measurement represents changes in the area of the imaged M phase across the MIT. Our measurements suggest the MIT in NNO is a broad transition from a paramagnetic (PM) non-Fermi-Liquid (NFL) metallic phase to an antiferromagnetic (AFM) insulating phase. The broadening is strain driven.

II. RESULTS AND DISCUSSION

A high-quality epitaxial thin film of NNO with dimensions 2.9 mm × 2.1 mm was grown on a LAO (100) substrate using pulsed laser deposition (PLD) [for details, see the Supplemental Material SI-1(I) [32]]. The film was grown with thickness variation along the film's width. The average thickness of the film was 50 ± 14 nm. Fig. 1(a) shows XRD $\theta-2\theta$ plot of the NNO/LAO (100) film. X-ray diffraction (XRD) shows the LAO substrate and the NNO peak, indicating phase purity and epitaxial film growth along the (100) direction. XRD-ω, ϕ scan measurements also show high crystalline quality in our NNO/LAO sample [for details, see SI-1(II) [32]]. Along with SF-MOI, $R(T)$ measurements were performed using two probe measurement techniques. Technical constraints related to performing both measurements in the same setup prevented the use of four-probe measurements

---

[*] dsrana@iiserb.ac.in

[†] satyajit@iitk.ac.in

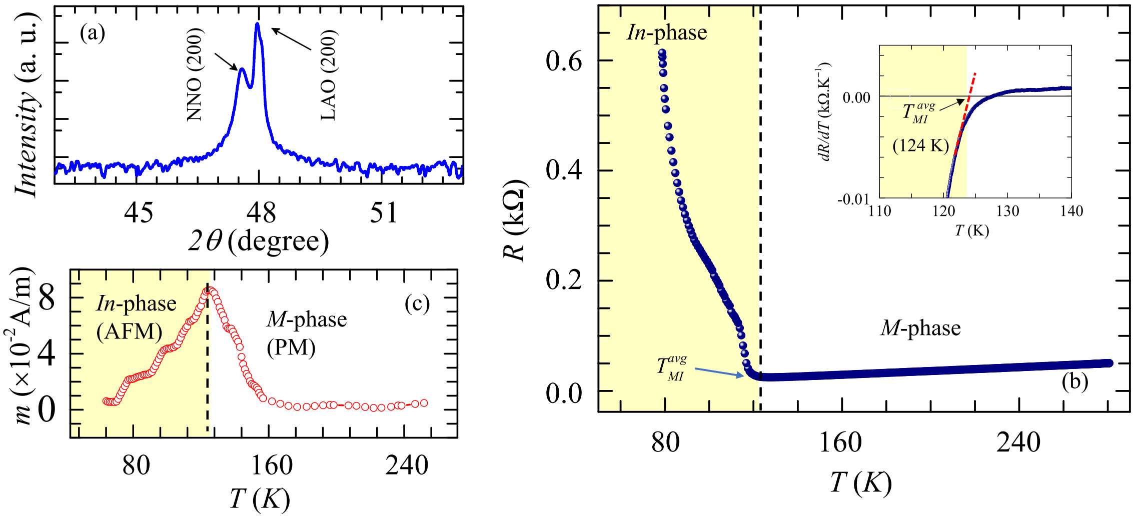

FIG. 1. (a) XRD $\theta-2\theta$ plot of the NNO/LAO (100) film. (b) $R\ (T)$ during the cooling cycle with a constant current of 5 mA. Inset shows dR/dT to determine MIT temperature. The yellow shaded region below 124 K corresponds to *In* phase (see text for details). (c) Magnetization versus T, $m\ (T)$, of the NNO film with an applied field of 1 kOe during cooling. Note that $m(T)$ of the bare LAO substrate was subtracted from $m(T)$ of NNO/LAO.

for $R(T)$. We find that by comparing two- and four-probe measurements, the contact resistance was ∼10 mΩ which is much smaller than the lowest resistance of the film of 25 Ω at the metal-insulator transition T, thereby validating the use of two-probe $R(T)$ measurements. The $R(T)$ measured with 5 mA current while cooling the sample in Fig. 1(b) shows a rapid increase in R below ∼124 K. While cooling from 280 K, we see a positive temperature coefficient of resistivity (TCR, dR/dT) with average resistivity $\rho_{280\,K} = 1.8\ \mu\Omega$ m. The positive TCR and an extrapolated nonzero resistivity at 0 K, $\rho_{0\,K} = 0.4\ \mu\Omega$ m (discussed later) identifies an M-phase region in Fig. 1(b). We identify the average mean-field MIT temperature, $T_{MI}^{\text{avg}} = 124$ K, from the low-temperature TCR curve [see inset Fig. 1(b)]. Below 124 K, the TCR is negative, suggesting the onset of an *In* phase [shaded region in Fig. 1(b)]. The temperature-dependent magnetization, $m(T)$ in Fig. 1(c), shows the NNO film is paramagnetic (PM) at $T > 160$ K. While field cooling in 1 kOe, the strong decrease in $m(T)$ below 124 K suggests a dominance of AFM interactions. It is known that NNO has unusual AFM order along $q = (\frac{1}{2},\ 0,\ \frac{1}{2})$ with respect to the orthorhombic unit cell and an up-up-down-down ferromagnetic (FM) stacking along the simple cubic (1,1,1) direction [26,33]. Thus, the NNO film displays a competition between FM and AFM interactions near 124 K, with the latter dominating at low T.

Figures 2(a) shows the optical image of the film with electrical contacts shown schematically. Fig. 2(b) shows the thickness profile $t(x)$ measured along the white dashed line (x) in Fig. 2(a) (Dektak XT advanced surface profilometer). The inset of Fig. 2(b) shows the different regions (A, B, C, D, and E) in the film with nearly similar average thickness.

To visualize current distribution in NNO film across T_{MI}^{avg}, we use the differential self-field magneto-optical imaging (SF-MOI) technique [34–36] [see SI-1(III) for details of the method [32]]. The SF-MOI technique measures the spatial distribution of the z component of the self-field, viz., $B^Z_{Self}(x, y)$ [where (x, y) are co-ordinates on the film plane, and z is perpendicular to it], generated by the current (I) sent in the film. Figure 2(c) shows a schematic of $B^Z_{\text{Self}}(x)$ profile (along the x axis) for uniform I along the y axis. The orange and light blue arrows represent positive and negative $B^Z_{\text{Self}}(x)$, respectively, and the arrow height represents the magnitude of $B^Z_{\text{Self}}(x)$. The inset of Fig. 2(d) is a typical SF-MOI image of $B^Z_{\text{Self}}(x, y)$ across the NNO film ($I = 15$ mA and $T = 165$ K). The white and black contrast in the image represents the maximum positive and negative $B^Z_{\text{Self}}(x)$ values, respectively. The measured $B^Z_{\text{Self}}(x)$ profile (along the line in inset) in Fig. 2(d) has a shape that is characteristic of a uniform current distribution (see Fig. 2 of Ref. [37]). Using an established numerical inversion algorithm [38], the current density distribution $J(x, y)$ across the film is determined by numerically inverting $B^Z_{\text{Self}}(x, y)$.

The $B^Z_{Self}(x, y)$ distribution across the M phase in the film at 174 K [viz. M-phase region in Fig. 1(b)] is shown in Fig. 3(a). Fig. 3(b) shows the $B^Z_{\text{Self}}(x)$ profile along the red dashed line in Fig. 3(a) [at other T, $B^Z_{\text{Self}}(x)$ is measured along the same line]. The $B^Z_{\text{Self}}(x)$ profile shows uniform current flow across the film at 174 K ($> T_{MI}^{\text{avg}}$). The measured profile and images remain similarly well above $T_{MI}^{\text{avg}} = 124$ K. However, near T_{MI}^{avg} [M-phase region in Fig. 1(b)], the $B^Z_{\text{Self}}(x)$ profile in Fig. 3(c) develops extra wiggles. Around $T_{MI}^{\text{avg}} (= 124$ K), near the top left of the SF-MOI image (circled) in Fig. 3(a), we see the development of a faint triangular-shaped feature, which becomes more pronounced at 121 K. Deep in the *In*-phase region, viz., for $T < T_{MI}^{\text{avg}}$, the triangular-shaped feature becomes more prominent. The $B^Z_{\text{Self}}(x)$ profile at 118 K in Fig. 3(d) shows the modulation across the sides of the triangular region. Reducing T, Fig. 3(a) shows that the triangular region expands deeper into the film and the left edge of the triangle expands across the left side of the film [see the evolution from 121 to 65 K in Fig. 3(a)]. In comparison, the right edge of

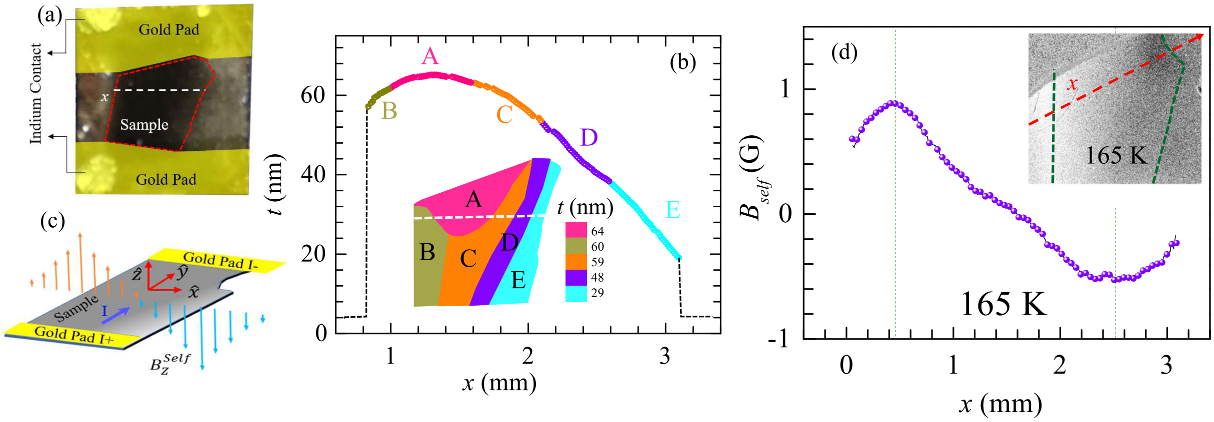

FIG. 2. (a) Optical image of the $NdNiO_3$ thin-film on the LAO substrate with the Cr (5 nm)/Au (50 nm) pad. The red dash shows the sample boundary. (b) Thickness variation of the sample along the white dashed line (x) of (a). Black dashed lines are two side edges of the sample, where we have cut out the film to provide sharp edges. Inset shows the schematic map of the average thickness in different regions (A, B, C, D, and E) of the sample. The average thickness is represented by a different color code in the schematic map of the sample, and the white dashed line represents the same line [as in (a)] along which thickness profile is measured. (c) Schematic of the self-field distribution $B^Z_{\rm Self}(x)$ (orange and light blue vertical arrow) due to uniform current flow through the sample (the sample shape in the schematic is kept identical to the actual contours of the film used in our experiment) and (d) shows experimentally observed $B^Z_{\rm Self}(x)$ distribution along the red dashed line in SF-MOI of the film shown in the inset of (d) at 165 K. Dark green dashes are the edges of the sample.

the triangle does not move much with reducing T. The $B^Z_{\rm Self}(x)$ behavior with T is related to a significant redistribution of current in the film below $T^{\rm avg}_{MI}$.

Figure 3(f) shows the $J(x,y)$ map determined from the corresponding $B^Z_{\rm Self}(x,y)$ images. The orange and green contrast in Fig. 3(f) corresponds to the film's high and low $J(x,y)$ regions, respectively. In the M-phase region at 174 K [Fig. 3(f)], the flat $J(x)$ profile in Fig. 3(g) shows a uniform $J(x,y)$ distribution across the film. This feature is retained up to $T^{\rm avg}_{MI}$. Below $T^{\rm avg}_{MI}$, current crowding begins to set in

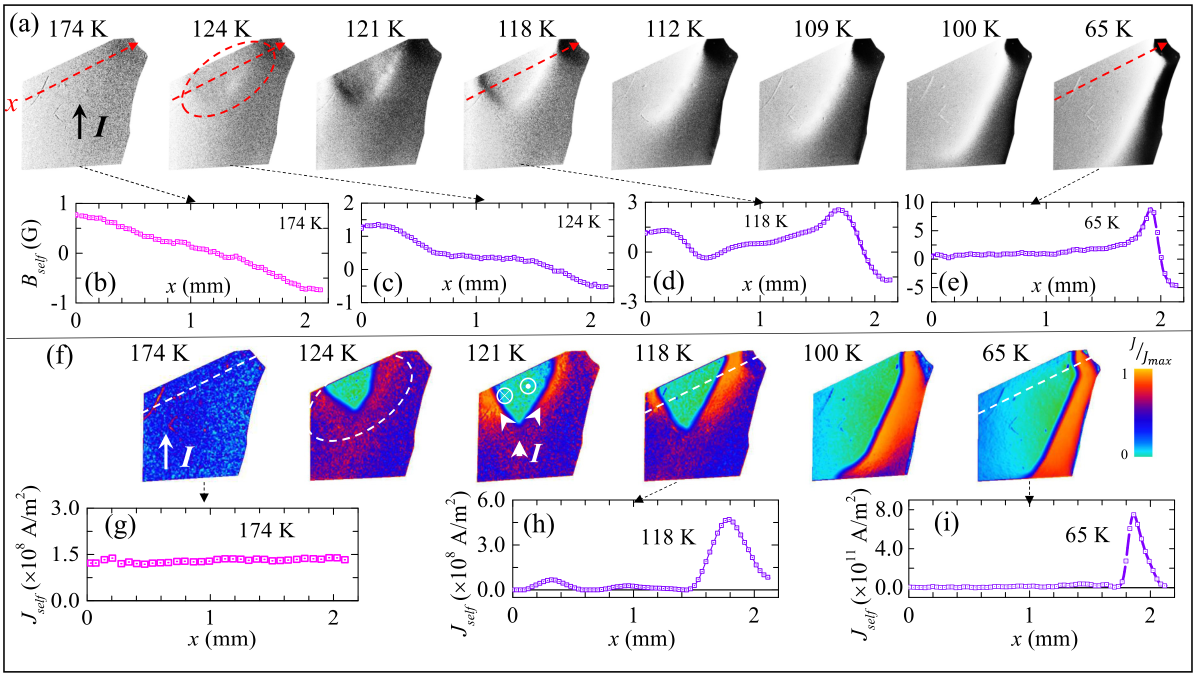

FIG. 3. (a) SF-MOI images of the sample taken at different temperatures with a current of 15 mA flowing through it. The black arrow in the image at 174 K indicates the current flow direction within the sample. (b)–(e) The line scans of $B^Z_{\rm Self}(x)$ profile along the red dashed arrow for images at 174, 124, 118, and 65 K, respectively. (f) Current density $J(x,y)$ map across the sample for different temperatures. The arrow in the figure of 174 K shows the I direction. The arrows in 121 K show the bifurcation of current at the triangular region. The symbols $\otimes$, $\odot$ near the edges of the triangle represent $B^Z_{\rm Self}$ pointing either in or out of the page plane, respectively. (g)–(i) $J(x)$ profile along a white dashed line for images at 174, 118, 65 K, respectively. The $J_{\rm max}$ in the color bar of (f) is the peak in $J(x)$ profile in (i). The $J(x,y)$ distributions in the images [(f)] have all been normalized by $J_{\rm max}$ and then colored. See text for details.

the NNO film. At 124 K, there are faint reddish regions with enhanced $J(x, y)$ [see inside the white dashed circle in Fig. 3(f)] around the edges of the triangular-shaped (greenish) region in Fig. 3(f). The current avoids flowing inside the greenish triangular region, and hence there is crowding along its edges where J is high. At lower T, triangular region expands, and current accumulation around the triangle edges becomes larger [see the orange regions in Fig. 3(f), 118 K]. The greenish triangular regions are the In phase with high resistivity nucleated at T_{MI}^{avg}. The appearance of the In phase over the entire greenish region of the sample is quite sharp and abrupt at T_{MI}^{avg} suggesting a first-order transition. As the In phase appears, the J in this region is swept out, and it accumulates around the edges of the triangular region. Below 124 K, the triangular region with an In phase (current free region) causes the current flow to split into two separate streams [cf. arrows Fig. 3(f), 121 K] along the sides of the triangle. Due to the two streams, the orientation of the B_{Self}^{Z} (right-hand rule) is opposite along the two sides of the triangle [cf. Fig. 3(f), 121 K]. This is seen as bright and dark contrasts in B_{Self}^{Z} images along the two adjacent edges of the triangle [e.g., see the 118 K, 121 K B_{Self}^{Z} image in Fig. 3(a)]. The movie in SI-2 of the Supplemental Material [32] shows in grayscale the evolution of the accumulation $B_{\mathrm{Self}}^{Z}(x, y)$ across the sample at different T. Fig. 3(f) shows that at 65 K ($\ll T_{MI}^{\mathrm{avg}}$) while almost the entire film has transformed into an insulating state (dark green region); however, there is a narrow orange sliver near the right edge of the film with large $J(\sim 10^{11}\ \mathrm{A\ m^{-2}})$, which is still metallic (orange region). Significant joule heating from this M sliver along with long image acquisition times coupled prevented imaging under isothermal conditions below 65 K. It may be worth mentioning here that in order to color our $J(x, y)$ images, we divided the range of current density values into separate bins, where each bin corresponding to a range of current density values was ascribed a specific color. Thus, this discretization scheme and the coloring choice resulted in some regions appearing as sharp boundaries in the colored images of the $J(x, y)$ distribution. Despite the impression of sharp boundaries in the colored images, the current density profile [e.g., see Fig. 3(h)] shows that the J changes smoothly rather than abruptly across such boundaries.

In NNO, two processes compete: charge hopping across $3d$ levels of Ni, which is governed by the charge transfer energy (Δ), and hybridization of O $2p$ and Ni $3d$ levels governed by the hybridization strength W [39,40]. In general, the strain-thickness relationship in nickelates is responsible for lifting the degeneracy of the e_g orbital and leads to orbital polarization, which in turn controls the MIT [11,30,41–45]. Recent studies reveal a rich phase diagram in NNO consisting of the paramagnetic metal (PM)–NFL phase, the PM-FL phase, and the AFM-insulator phase [11]. It has been found that for fixed compressive strain, as the film dimensionality (viz., t) is reduced, enhanced correlation effects increase Δ (compared to W), and the T_{MI} increases, viz., favoring an In phase to appear at relatively higher T. On the other hand, an increase in compressive strain broadens Ni-O bandwidth, which enhances W (compared to Δ) resulting in a decrease of T_{MI},viz., favoring the M phase to prevail at low T. Studies in rare-earth nickelates have suggested a critical t_c [29,39] where for $t > t_c \sim 20$ u.c. strain effects dominate, resulting in decreasing T_{MI} with decreasing t [11,29,39]. Note that both sides of our film have $t(x) > t_c = 20$ NNO u.c. ($\sim$9 nm). Another alternate scenario that can produce a variation of MIT transition temperatures across the film could be related to the presence of regions with different crystalline quality, and there may also exist a variation of oxygen concentration across the film. We eliminate the possibility of the bad crystalline quality of the film, as XRD-ω, ϕ scan measurements in our NNO/LAO sample show high crystalline quality with homogeneous epitaxial film growth [for details, see SI-1(II) [32]]. Regarding oxygen deficiency in the film, it is worth recalling here that in nickelate films, oxygen deficiency is found in tensile-strained films [46], whereas we have compressively strained films. Also, our entire film was subjected to identical growth conditions, and hence it is unlikely that different regions of our film have different oxygen stoichiometry. Our electron probe microanalyzer (EPMA) measurements show that at the most, there may exist up to a 0.5–1% variation in oxygen concentration across the sample. Such very low fluctuation in oxygen concentration is not the source of the large difference in T_{MI} between the left and right sides of the film [for details, see SI-1(V) [32]]. In regions of the films where we observe minor oxygen concentration fluctuations, there is no discernable difference in the T_{MI} seen in SF-MOI.

Hence, strain effects will determine the local behavior of $T_{MI}(x)$ on both sides of the film [39], and there will be a minimal effect of the dimensionality and effect of oxygen stoichiometry on the T_{MI}. Our results suggest a competition between Δ and W. From the XRD peak positions [Fig. 1(a)], the lattice mismatch between NNO film and LAO substrate in the out-of-plane direction is $\sim$0.74%. Furthermore, the reciprocal space map (RSM) [47] about the asymmetric (301) Bragg's peak in Fig. 4(a) shows that the substrate and film's (301) peak lie on the same pseudomorphic line (cf. orange dashed line). The observed collinearity of peaks in the RSM indicates a forced matching of the in-plane lattice parameters of NNO and LAO. This suggests a fully compressed-strained state of the NNO film. Our results are explained based on the nonuniform distribution of local T_{MI} values due to thickness variation across the film [see inset of Fig. 2(b)]. The $t(x)$ profile in Fig. 2(b) (and inset) shows the film is thickest in region A. The film thickness in region B > C > D > E. At 300 K, the whole sample is metallic, and the current flows uniformly across the film [Fig. 3(f), 174 K]. Lowering $T < T_{MI}^{\mathrm{avg}}$, the In phase [green region in Fig. 3(f), 124 K] first forms over the entire triangular film region A [Fig. 2(b) inset] with the highest but uniform film thickness. With further lowering of T, the In phase spreads to region B followed by regions C and D [compare inset Fig. 2(b) with the evolution of the triangular region in Fig. 3(a) or the greenish region in Fig. 3(f)]. This continues until the entire current is localized in the thinnest right film edge [cf. region E in inset of Fig. 2(b)] of the film where the M phase persists [see orange, high J sliver in Fig. 3(f), 65 K]. It is well known that average compressive strain relaxes with increasing film thickness, i.e., approximately, average strain $e \propto \frac{1}{t}$. Fig. 4(b i) schematically shows an example of a MIT behavior in a film with a nonuniform average strain field $e(x, y)$ distribution. At high T the entire film is metallic. However, as discussed earlier, the presence of $e(x, y)$ causes the T_{MI} to vary locally across the film. As T is decreased,

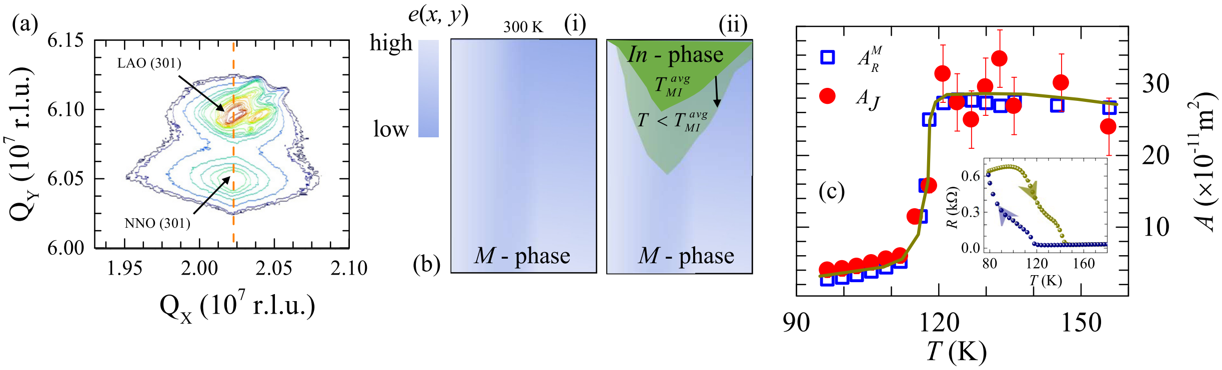

FIG. 4. (a) The reciprocal space map of $NdNiO_3$ thin film along the asymmetric (301) reflection of the LAO substrate. (b i) is a schematic example showing average strain $e\ (x, y)$ variation across the sample. At 300 K, the entire sample is in M phase. (b ii) shows the formation of In phase (dark green region) at T_{MI}^{avg} in the low-strain region and its spreading (light green region) across the high-strain regions of the MIT, $T < T_{MI}^{\text{avg}}$. (c) Average cross-sectional area (A) of the sample calculated from transport (A_R^M) and SF-MOI (A_J) measurements (errors in the data are of the order of symbol size). Inset shows $R(T)$ cooling and heating curve with a current of 5 mA, exhibiting significant hysteresis in MIT temperatures. The MIT temperature while heating is 148 K.

different regions of the film transform into the In phase when $T <$ local T_{MI} [see Fig. 4(b ii) at $T < T_{MI}^{\text{avg}}$]. Thus, the thickest film region A has the least average strain, and it has $T_{MI} \sim 124$ K $= T_{MI}^{\text{avg}}$. Due to progressively decreasing thickness in film regions B, C, D, and E, the progressively increasing strain in those regions result in T_{MI} (in region B) $> T_{MI}$ (in region C) $> T_{MI}$ (in region D) $> T_{MI}$ (in region E). Hence we observed sequential spreading of the In phase from region A to B, C, D, and E, respectively. To support our claim of strain field scenario, we have grown four uniform-thickness samples (35, 45, 60, 240 nm) with the same deposition conditions. Our XRD, RSM measurements show that the compressive strain in the films reduces progressively with increasing thickness [see SI-1(IV) [32]]. $R(T)$ measurements along with the above RSM results clearly show that higher compressive strain in uniform, low thickness nickelate thin films result in a lower T_{MI} compared to more relaxed thicker thin film where the $T_M \to T_{MI}^{\text{avg}}$ [see SI-1(IV) [32]].

Next, we show the change in $R(T)$ below T_{MI}^{avg} does not represent the increase in the average bulk resistivity of the film, as expected in MIT. Fig. 1(b) shows that for $T > T_{MI}^{\text{avg}}$ the metallic phase has a temperature-dependent average resistivity of the form $\rho(T) = \rho(0) + \beta T^n$, with $\rho(0) = 3.82(\pm 0.01) \times 10^{-7}\ \Omega\,\text{m}$ and $\beta = 1.99(\pm 0.01) \times 10^{-9}\ \Omega\,\text{m/K}$, and $n = 1.0 \pm 0.1$. The $n < 2$ suggests NFL behavior which is consistent with earlier reports on NNO film [11]. We now show that the increase in $R(T)$ below T_{MI}^{avg} is related to the narrowing down of the average film's cross-section area, which carries current. From $\rho(T)$ we calculate the T dependence of the average cross-section area [$A_R^M(T)$] of the metallic region, which is perpendicular to J, viz., $A_R^M(T) = \frac{\rho(T)L}{R(T)}$ where L is the length of the film [open blue square in Fig. 4(c)]. Also, directly from our $J(x, y)$ images of Fig. 3(f), we can estimate the T dependence of the average cross-sectional area perpendicular to the current flow $A_J(T)$ [closed red circle in Fig. 4(c)] [see SI-1(VI) [32]]. At low $T \ll T_{MI}^{\text{avg}}$, where there is less error in determining $A_J(T)$, we see a good match between $A_R^M(T)$ and $A_J(T)$. The close match between the $A_R^M(T)$ estimated from the $R(T)$ data using the above considerations and the $A_J(T)$ which have been measured directly from the self-field images validates the procedure used to calculate $A_R^M(T)$. This shows that the $R(T)$ behavior below T_{MI}^{avg} represents a change in the cross-sectional current-carrying area (viz., the M-phase region). Thus the M-phase area drops rapidly below T_{MI}^{avg} [Fig. 4(c)]. This observation, together with the strong hysteresis in $R(T)$ [see the inset of Fig. 4(c)], which corresponds to hysteresis in $A_R^M(T)$, suggests a first-order nature of the MIT in NNO film. Studies suggest unclarity about the nature of the MIT in nickelates and what affects it. Some studies indicate a first-order nature of the MIT [30,43,44,47–50], especially locally, while it could be second-order-like as seen in bulk measurements [14]. Our measurements show that the MIT in nickelates is a first-order-like transition. Due to the ever-present strain distribution in the film, there is a broad distribution of $T_{MI}(x, y)$ across the film. This results in the MIT occurring at slightly different local $T_{MI}(x, y)$ values across the film [Fig. 4(a)], albeit still a first-order transition locally. The feature we observe, viz., strain-induced broadening of the MIT showing smaller local first-order transitions, is reminiscent of the effect of disorder-induced broadening of a sharp order-disorder transition by formation of intermediate multiple smaller domains with order [51].

III. CONCLUSION

In conclusion, in the strongly correlated NNO on LAO film, the film's dimensionality (thickness), stoichiometry, and strain field are the major players in governing the behavior of the MIT. In our film with a thickness gradient, we show that there is a significant difference in the MIT temperature between the thick and thin portions of the film. Our investigations reveal that neither the film's dimensionality, which has a tendency to modify correlations and affect the MIT, nor the film's stoichiometric variations is responsible for this difference. We show that it is the local strain field that plays a dominant role in governing the features of the MIT, and it helps to control the spatial distribution of currents across a metal-insulator transition (MIT) in the film. Such studies could have important implications for strain-controlled applications involving such materials. More future studies are needed to understand the intriguing details of the MIT in such systems.

ACKNOWLEDGMENTS

S.S.B. acknowledges funding support from IIT Kanpur and the Department of Science and Technology (DST), India (Imprint-II programs). D.S.R. thanks DST Nanomission for financial support under Research Project No. SM/NM/NS-84/2016. S.G. acknowledges Council of Scientific and Industrial Research (CSIR), India for funding. S.S. acknowledges Prime Minister's Research Fellows (PMRF) Scheme of the Ministry of Human Resource Development, Govt. of India for funding support.

---

[1] N. Mott, Proc. R. Soc. A **382**, 1 (1982).
[2] V. Dobrosavljevic, N. Trivedi, and J. M. Valles, Jr., *Conductor Insulator Quantum Phase Transitions* (Oxford University Press, Oxford, UK, 2012).
[3] A. Möbius, Crit. Rev. Solid State Mater. Sci. **44**, 1 (2019).
[4] T. F. Rosenbaum, K. Andres, G. A. Thomas, and R. N. Bhatt, Phys. Rev. Lett. **45**, 1723 (1980).
[5] M. N. Alexander and D. F. Holcomb, Rev. Mod. Phys. **40**, 815 (1968).
[6] P. P. Edwards, T. V. Ramakrishnan, and C. N. R. Rao, J. Phys. Chem. **99**, 5228 (1995).
[7] M. Imada, A. Fujimori, and Y. Tokura, Rev. Mod. Phys. **70**, 1039 (1998).
[8] A. Mercy, J. Bieder, J. Íñiguez, and P. Ghosez, Nat. Commun. **8**, 1677 (2017).
[9] A. M. Haghiri-Gosnet and J. P. Renard, J. Phys. D: Appl. Phys. **36**, R127 (2003).
[10] M. L. Medarde, J. Phys. Condens. Matter **9**, 1679 (1997).
[11] E. Mikheev, A. J. Hauser, B. Himmetoglu, N. E. Moreno, A. Janotti, C. G. Van de Walle, and S. Stemmer, Sci. Adv. **1**, e1500797 (2015).
[12] J. S. Zhou, J. B. Goodenough, and B. Dabrowski, Phys. Rev. Lett. **94**, 226602 (2005).
[13] M. M. Qazilbash, M. Brehm, B.-G. Chae, P. C. Ho, G. O. Andreev, B.-J. Kim, S. J. Yun, A. V. Balatsky, M. B. Maple, F. Keilmann *et al.*, Science **318**, 1750 (2007).
[14] K. W. Post, A. S. McLeod, M. Hepting, M. Bluschke, Y. Wang, G. Cristiani, G. Logvenov, A. Charnukha, G. X. Ni, P. Radhakrishnan *et al.*, Nat. Phys. **14**, 1056 (2018).
[15] M. Fath, S. Freisem, A. A. Menovsky, Y. Tomioka, J. Aarts, and J. A. Mydosh, Science **285**, 1540 (1999).
[16] A. S. McLeod, E. van Heumen, J. G. Ramirez, S. Wang, T. Saerbeck, S. Guenon, M. Goldflam, L. Anderegg, P. Kelly, A. Mueller *et al.*, Nat. Phys. **13**, 80 (2017).
[17] G. Mattoni, P. Zubko, F. Maccherozzi, A. J. H. van der Torren, D. B. Boltje, M. Hadjimichael, N. Manca, S. Catalano, M. Gibert, Y. Liu *et al.*, Nat. Commun. **7**, 13141 (2016).
[18] Z. Yang, C. Y. Ko, and S. Ramanathan, Annu. Rev. Mater. Res. **41**, 337 (2011).
[19] Z. Liao, N. Gauquelin, R. J. Green, K. Müller-Caspary, I. Lobato, L. Li, S. Van Aert, J. Verbeeck, M. Huijben, M. N. Grisolia *et al.*, Proc. Natl. Acad. Sci. USA **115**, 9515 (2018).
[20] G. Catalan, Phase Transit. **81**, 729 (2008).
[21] J. Liu, M. Kargarian, M. Kareev, B. Gray, P. J. Ryan, A. Cruz, N. Tahir, Y.-D. Chuang, J. Guo, J. M. Rondinelli *et al.*, Nat. Commun. **4**, 2714 (2013).
[22] R. Jaramillo, S. D. Ha, D. M. Silevitch, and S. Ramanathan, Nat. Phys. **10**, 304 (2014).
[23] J. B. Torrance, P. Lacorre, A. I. Nazzal, E. J. Ansaldo, and C. Niedermayer, Phys. Rev. B **45**, 8209 (1992).
[24] M. K. Hooda and C. S. Yadav, Phys. B (Amsterdam, Neth.) **491**, 31 (2016).
[25] S. Catalano, M. Gibert, J. Fowlie, J. Íñiguez, J. M. Triscone, and J. Kreisel, Rep. Prog. Phys. **81**, 046501 (2018).
[26] J. L. García-Muñoz, J. Rodríguez-Carvajal, and P. Lacorre, Phys. Rev. B **50**, 978 (1994).
[27] J. Rodríguez-Carvajal, S. Rosenkranz, M. Medarde, P. Lacorre, M. T. Fernandez-Díaz, F. Fauth, and V. Trounov, Phys. Rev. B **57**, 456 (1998).
[28] C. Piamonteze, H. C. N. Tolentino, A. Y. Ramos, N. E. Massa, J. A. Alonso, M. J. Martinez-Lope, and M. T. Casais, Phys. B (Amsterdam, Neth.) **320**, 71 (2002).
[29] J. J. Peng, C. Song, M. Wang, F. Li, B. Cui, G. Y. Wang, P. Yu, and F. Pan, Phys. Rev. B **93**, 235102 (2016).
[30] D. Kaur, J. Jesudasan, and P. Raychaudhuri, Solid State Commun. **136**, 369 (2005).
[31] R. S. Bisht, S. Samanta, and A. K. Raychaudhuri, Phys. Rev. B **95**, 115147 (2017).
[32] See Supplemental Material at http://link.aps.org/supplemental/10.1103/PhysRevB.105.085143 for growth conditions, structural and compositional characterisations of the thin film, transport studies at different thickness of the film, and a brief description of the self-field magneto-optical-imaging (SF-MOI) technique.
[33] V. Scagnoli, U. Staub, A. M. Mulders, M. Janousch, G. I. Meijer, G. Hammerl, J. M. Tonnerre, and N. Stojic, Phys. Rev. B **73**, 100409(R) (2006).
[34] S. S. Banerjee, S. Goldberg, A. Soibel, Y. Myasoedov, M. Rappaport, E. Zeldov, F. de la Cruz, C. J. van der Beek, M. Konczykowski, T. Tamegai *et al.*, Phys. Rev. Lett. **93**, 097002 (2004).
[35] A. Kumar, S. Ghosh, T. Tamegai, and S. S. Banerjee, Phys. Rev. B **101**, 014502 (2020).
[36] A. Jash, A. Kumar, S. Ghosh, A. Bharathi, and S. S. Banerjee, Sci. Rep. **11**, 7445 (2021).
[37] D. T. Fuchs, E. Zeldov, M. Rappaport, T. Tamegai, S. Ooi, and H. Shtrikman, Nature (London) **391**, 373 (1998).
[38] R. J. Wijngaarden, H. J. W. Spoelder, R. Surdeanu, and R. Griessen, Phys. Rev. B **54**, 6742 (1996).
[39] L. Wang, S. Ju, L. You, Y. Qi, Y.-w. Guo, P. Ren, Y. Zhou, and J. Wang, Sci. Rep. **5**, 18707 (2015).
[40] A. V. Boris, Y. Matiks, E. Benckiser, A. Frano, P. Popovich, V. Hinkov, P. Wochner, M. Castro-Colin, E. Detemple, V. K. Malik *et al.*, Science **332**, 937 (2011).
[41] I. I. Mazin, D. I. Khomskii, R. Lengsdorf, J. A. Alonso, W. G.

Marshall, R. M. Ibberson, A. Podlesnyak, M. J. Martínez-Lope, and M. M. Abd-Elmeguid, Phys. Rev. Lett. **98**, 176406 (2007).

[42] S. Johnston, A. Mukherjee, I. Elfimov, M. Berciu, and G. A. Sawatzky, Phys. Rev. Lett. **112**, 106404 (2014).

[43] A. Kumar, P. Singh, D. Kaur, J. Jesudasan, and P. Raychaudhuri, J. Phys. D: Appl. Phys. **39**, 5310 (2006).

[44] T. Shao, Z. Qi, Y. Wang, Y. Li, M. Yang, and C. Hu, Appl. Surf. Sci. **399**, 346 (2017).

[45] G. Catalan, R. M. Bowman, and J. M. Gregg, Phys. Rev. B **62**, 7892 (2000).

[46] S. Heo, C. Oh, J. Son, and H. M. Jang, Sci. Rep. **7**, 4681 (2017).

[47] R. Rana, P. Pandey, V. E. Phanindra, S. S. Prabhu, and D. S. Rana, Phys. Rev. B **97**, 045123 (2018).

[48] D. Kumar, K. P. Rajeev, A. K. Kushwaha, and R. C. Budhani, J. Appl. Phys. **108**, 063503 (2010).

[49] J. Son, B. Jalan, A. P. Kajdos, L. Balents, S. J. Allen, and S. Stemmer, Appl. Phys. Lett. **99**, 192107 (2011).

[50] P. H. Xiang, N. Zhong, C. G. Duan, X. D. Tang, Z. G. Hu, P. X. Yang, Z. Q. Zhu, and J. H. Chu, J. Appl. Phys. **114**, 243713 (2013).

[51] Y. Imry and S.-k. Ma, Phys. Rev. Lett. **35**, 1399 (1975).